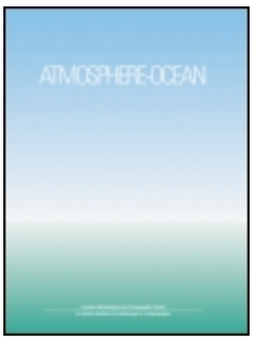

Atmosphere-Ocean

ISSN: 0705-5900 (Print) 1480-9214 (Online) Journal homepage: https://www.tandfonline.com/loi/tato20

Upper-boundary effects in a contour dynamics/ surgery model of the polar stratospheric vortex

John Fyfe & Xiaohong Wang

To cite this article: John Fyfe & Xiaohong Wang (1997) Upper-boundary effects in a contour dynamics/surgery model of the polar stratospheric vortex, Atmosphere-Ocean, 35:2, 189-207, DOI: 10.1080/07055900.1997.9649591

To link to this article: https://doi.org/10.1080/07055900.1997.9649591

Published online: 19 Nov 2010.

Upper-Boundary Effects in a Contour Dynamics/Surgery Model of the Polar Stratospheric Vortex

John Fyfe
Canadian Centre for Climate Modelling and Analysis
Atmospheric Environment Service
University of Victoria, Victoria, British Columbia,
Canada V8W 2Y2

and

Xiaohong Wang
Department of Computer Science
University of Victoria, Victoria, British Columbia, Canada

[Original manuscript received 24 January 1996; in revised form 11 December 1996]

ABSTRACT *Considering the influence of the upper-boundary on wave breaking in a Boussinesq environment, we compare ultra-high resolution numerical simulations of a topographically forced polar stratospheric vortex using: 1) a rigid upper-boundary condition (following Dritschel and Saravanan, 1994) and 2) a vertical sponge (preventing spurious reflection of upward propagating waves). In 1) both local (to the forcing) and remote breaking is evidenced for weak forcing while only local breaking is observed for sufficiently strong forcing. In 2) remote breaking is absent and local breaking, which occurs for sufficiently strong forcing, has quite a different character to that seen in 1). Compressibility effects are also discussed.*

RÉSUMÉ *Considérant l'influence de la limite supérieure sur le déferlement des ondes dans un environnement de Boussinesq, nous comparons, dans le cas d'une topographie forcée pour un tourbillon circumpolaire stratosphérique, des simulations numériques en utilisant : 1) des conditions rigides pour les limites supérieures verticals (voir Dritschel et Saravanan, 1994) et 2) une couche éponge (empêchant toute réflexion indésirable des ondes de propagation ascendantes). En 1) les deux déferlements local (dû au forçage) et éloigné sont mis en évidence pour un forçage faible, toutefois, on observe seulement un déferlement local pour un forçage suffisamment fort. En 2) le déferlement éloigné est absent tandis que le déferlement local, qui se présente lors d'un forçage suffisamment fort, possède une caractéristique différente que celle vue en 1). Les effets de compressibilité sont aussi discutés.*

ATMOSPHERE-OCEAN 35 (2) 1997, 189–207 0705-5900/97/0000-0189$1.25/0

1 Introduction

This study is primarily motivated by the 1994 work of Dritschel and Saravanan (hereafter DS). DS used a three-dimensional quasi-geostrophic contour dynamics/surgery numerical model to study the response of a barotropic vortex to topographic forcing of varying amplitude. The main result of DS was that for either Boussinesq or compressible flow two regimes of wave breaking exist, namely, *local* wave breaking occurring near the lower boundary for strong topographic forcing and *remote* wave breaking occurring at the upper levels for weaker topographic forcing. Local wave breaking is due directly to the topography, is not very sensitive to the upper boundary condition (in the sense that when the domain height is halved the local breaking is preserved) and apparently has a shielding effect on the upper levels. Remote wave breaking is due to vertical transport of wave activity from the bottom to the top of the model, is sensitive to the upper boundary condition (in the sense that when the domain height is halved remote breaking vanishes) and is coupled with the compressibility effect when compressibility is involved. It is the upper boundary condition sensitivities, for Boussinesq flow in particular, that we set out in Section 3 to investigate by replacing the model's rigid lid with a vertical sponge. We mainly focus on a Boussinesq fluid in order to accentuate the influence of the upper boundary condition when that influence is important. In Section 4 we expand the discussion to include density effects.

This study is also motivated by the 1990 work of Fyfe and Held who, using a barotropic pseudo-spectral numerical model, illustrated a mechanism by which horizontally-propagating planetary waves spontaneously break even in the absence of a so-called "critical layer" (a similar mechanism for vertically-propagating internal waves was described by Dunkerton, 1981). It is our intention, in a future study, to consider the spontaneous breakdown of *vertically* propagating planetary waves using the ultra-high resolution model of DS. To do so, however, requires the implementation and testing of a vertical sponge, hence the present study.

2 Three-dimensional quasi-geostrophic contour dynamics/surgery

We now briefly introduce some of the ingredients of the numerical model. A much more detailed account is contained in DS.

a *Quasi-geostrophic potential vorticity*

For inviscid fluids we have conservation of quasi-geostrophic potential vorticity (see Pedlosky, 1987 or Andrews et al., 1987):

$$q = \nabla^2 \psi + \frac{1}{\rho_0} \frac{\partial}{\partial z} \left(\rho_0 \frac{f_0^2}{N_0^2} \frac{\partial \psi}{\partial z} \right) \tag{1}$$

in every infinitesimal layer of fluid when advected by the geostrophic velocity field $u = -\partial\psi/\partial y$ and $v = \partial\psi/\partial x$ [$\psi(x, y, z, t)$ is the geostrophic streamfunction, $\rho_0(z)$ is the background density, $f_0 = 2\Omega$ is the (constant) Coriolis parameter and $N_0(z)$ the background Brunt-Väisälä frequency]. Here we consider a Boussi-

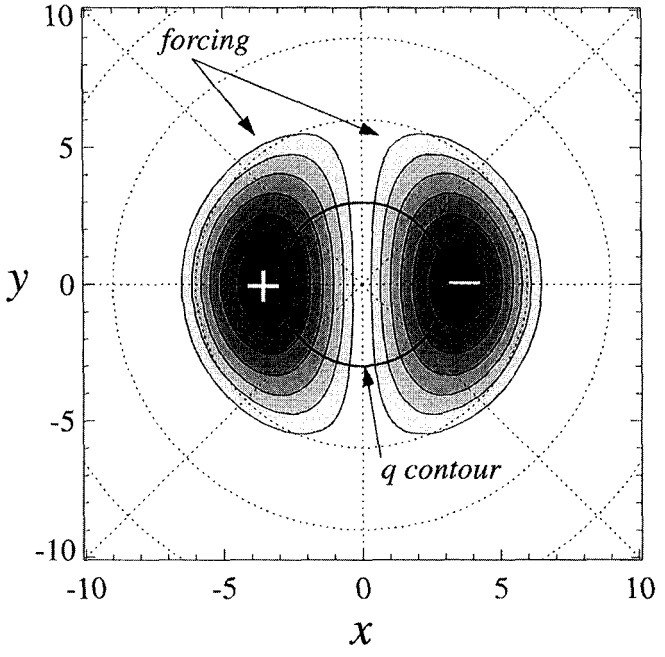

Fig. 1 Plan view of the initial vortex (bold solid line) where q is equal to 5.2π inside and 3.6π outside the bold solid line. Also shown is the topographic forcing function $-f_0\eta(x, y)$ (shaded). The centre of the plot is the "North Pole" and lines of "latitude" and "longitude" are dotted.

nesq fluid with constant density stratification and Brunt-Väisälä frequency given by $N_0 = \sqrt{g^2/c_pT_0}$ ($T_0 = 210$ K) and we non-dimensionalize with the time, vertical- and horizontal-length scales, $S = 4\pi/f_0 = 1$ day, $H = RT_0/g \approx 6.14$ km and $L = N_0H/f_0 \approx 902$ km, respectively. From here on all variables are nondimensional except when circumflexed. Numerical solutions are obtained by vertically discretizing into n layers (ranging from 20 to 66 depending on the particular experiment) of equal thickness with all dynamical variables (i.e., q and velocity) residing at the mid-layer levels. We deal with the horizontal discretization in Subsection c.

b *Initial and boundary conditions*

The geometry is a polar-cap f-plane, meaning that the fluid is unbounded horizontally with the centre of the domain ($r \equiv \sqrt{x^2 + y^2} = 0$) corresponding to the North Pole. The initial condition is a barotropic cylindrical polar vortex, i.e.,

$$q = \begin{cases} 5.2\pi & \text{for } r < r_0 \\ 3.6\pi & \text{for } r > r_0 \end{cases} \tag{2}$$

(see Fig. 1) and the top ($z = z_T$) and bottom ($z = z_B$) kinematic boundary conditions are:

$$\frac{f_0^2}{N_0^2}\frac{\partial \psi}{\partial z} = \begin{cases} 0 & \text{at } z = z_T \\ -f_0\eta(x, y) & \text{at } z = z_B. \end{cases} \tag{3}$$

In this study $\hat{z}_B = 12$ km (nominally the tropopause) and $\hat{z}_T$ ranges from 48 to 144 km, depending on the particular experiment. In polar coordinates, the topographic shape (see Fig. 1) is given by $\eta(r, \theta) = \eta_0 J_1(\kappa r)\mathcal{F}(r)\cos\theta$ where η_0 is the topographic amplitude (ranging from 0.04 to 0.60 depending on the particular experiment), $\kappa = 1.6/r_0$ with $r_0 = 3$ and $\mathcal{F}(r)$ is the taper function:

$$\mathcal{F}(r) = \begin{cases} 1 & \text{for } r \leqslant 5 \\ \cos\left(\pi \dfrac{r-5}{5}\right) & \text{for } 5 < r \leqslant 7.5 \\ 0 & \text{for } 7.5 < r. \end{cases} \tag{4}$$

c *Contour dynamics/surgery*

Unlike the usual approach to horizontal discretization, contour dynamics "divides space into a finite number of dynamic regions and discretizes the contours separating distinct regions of vorticity" (Dritschel, 1989). Contour dynamics exploits the fact that if vorticity is materially-conserved and piecewise-uniform then the instantaneous vorticity contour configuration completely determines the velocity field (e.g. see the Green function calculation in Eq. (18) of DS). Further, the velocity field at the contour positions is all that is required to evolve the system forward in time. Specifically, contour positions $\mathbf{x} = (x, y)$ are changed on the basis of the horizontal velocity field $\mathbf{u} = (u, v)$ via the particle equation,

$$\frac{d\mathbf{x}}{dt} = \mathbf{u}. \tag{5}$$

In a sense, the dimension of the mathematical system is reduced by one, allowing for extended (in time) high resolution (in space) simulations. Space and time resolution is pushed further with the algorithms of contour surgery which dynamically control regions of extreme and fast-growing curvature. For more on the contour dynamics/surgery technique and applications the interested reader is referred to Dritschel, 1988; Dritschel, 1989; Polvani and Plumb, 1992; Waugh, 1993; Dritschel and Saravanan, 1994.

d *Vertical sponge*

In the region of the vertical sponge (i.e., $z_S \leqslant z \leqslant z_T$) the velocity field is adjusted with a "forcing" velocity $\mathbf{u_F}$ and a "restoring" velocity $\mathbf{u_R}$:

$$\begin{gathered} \frac{d\mathbf{x}}{dt} = \mathbf{u} + \mathbf{u_F} + \mathbf{u_R} \quad \text{with} \\ \mathbf{u_F} \equiv \mu(z, t)\mathbf{k} \times \mathbf{u}^{\mathbf{bt}} \quad \text{and} \quad \mathbf{u_R} \equiv -\alpha(z)\frac{r}{2}\mathbf{i} \end{gathered} \tag{6}$$

where $\mathbf{k}$ and $\mathbf{i}$ are unit vectors in the vertical and radial directions, respectively, and

$\mathbf{u}^{\mathbf{bt}}$ is the barotropic component of $\mathbf{u}$. It is important to note that both the "forcing" and "restoring" velocities are by design irrotational and as such neither introduces any external vorticity into the system. The magnitude $\mu(z,t)$ of $\mathbf{u_F}$ is determined by:

$$\int_{\mathcal{R}} (\mathbf{u_F} + \mathbf{u_R}) \cdot \nabla q \, d\mathcal{R} = \int_{\mathcal{R}} \frac{\alpha(z)}{\rho_0} \frac{\partial}{\partial z} \left\{ \rho_0 \frac{f_0^2}{N_0^2} \frac{\partial}{\partial z} (\psi - \tilde{\psi}) \right\} d\mathcal{R}, \tag{7}$$

where $\mathcal{R}$ is some region enclosing the contour, $\tilde{\psi}$ is a prescribed equilibrium streamfunction and $\alpha(z)$ is a "Newtonian damping" coefficient defined as

$$\alpha(z) = \begin{cases} \alpha_T \{ e^{-4[(z_T - z)/(z_T - z_S)]^2} - e^{-4} \} & \text{for } z_S \leqslant z \leqslant z_T \\ 0 & \text{for } z < z_S. \end{cases} \tag{8}$$

In words, Eq. (7) equates the advection of q by $\mathbf{u_F} + \mathbf{u_R}$ to the damping of vertical gradients of any temperature anomalies (i.e., $\frac{\partial}{\partial z}(\psi - \tilde{\psi})$) that arise. The equilibrium streamfunction $\tilde{\psi}(x,y,z)$ is taken to be the initial state streamfunction. In Eq. (8) note that $\alpha[(z_T + z_S)/2] \approx \alpha_T e^{-1}$ and $\alpha(z_T) \approx \alpha_T$. Here we take the bottom of the vertical sponge to be at $\hat{z}_S = 48$ km (nominally the stratopause) and after considerable experimentation, to be described next, set $\hat{z}_T = 72$ km (giving about a four scale height vertical sponge) and $\alpha_T = 1.6$.

1 VERTICAL SPONGE SENSITIVITY EXPERIMENTS

The vertical sponge thickness, $z_T - z_S$, and maximum relaxation rate α_T (hereafter relaxation rate) quoted above have been determined by trial and error using a vertical sponge under a weak forcing condition (i.e., $\eta_0 = 0.15$). The rationale for the weak forcing, at this stage, is that since there is no wave breaking (and the response is nearly linear) the simulations are relatively easy to interpret and economical. Consider Fig. 2, which for a range of relaxation rates shows the total wave activity (or pseudomomentum) density (hereafter total wave activity) when $\hat{z}_T = 120$ km (giving about a twelve scale height vertical sponge). Wave activity is a useful diagnostic for monitoring the mean-square amplitude of wavy disturbances relative to a circularly symmetric basic flow (see DS Appendix B for a full definition). In the $\alpha_T = 0$ (no vertical sponge) simulation we see initial upward propagation which after apparent multiple boundary reflections leads to a complicated and unsteady vertical structure. On the other hand, when $1.6 \leqslant \alpha_T \leqslant 3.2$ the boundary reflections are largely brought under control. As seen in Fig. 3, dropping the top of the vertical sponge to $\hat{z}_T = 72$ km (giving about a four scale height thickness and a much reduced computational load) does not seriously compromise the absorbing ability of the vertical sponge. It is on the basis of these experiments, and others with larger topographic amplitudes (see Table 1 for a summary of all experiments conducted), that we have selected $\hat{z}_T = 72$ km and $\alpha_T = 1.6$ as our main vertical sponge parameters.

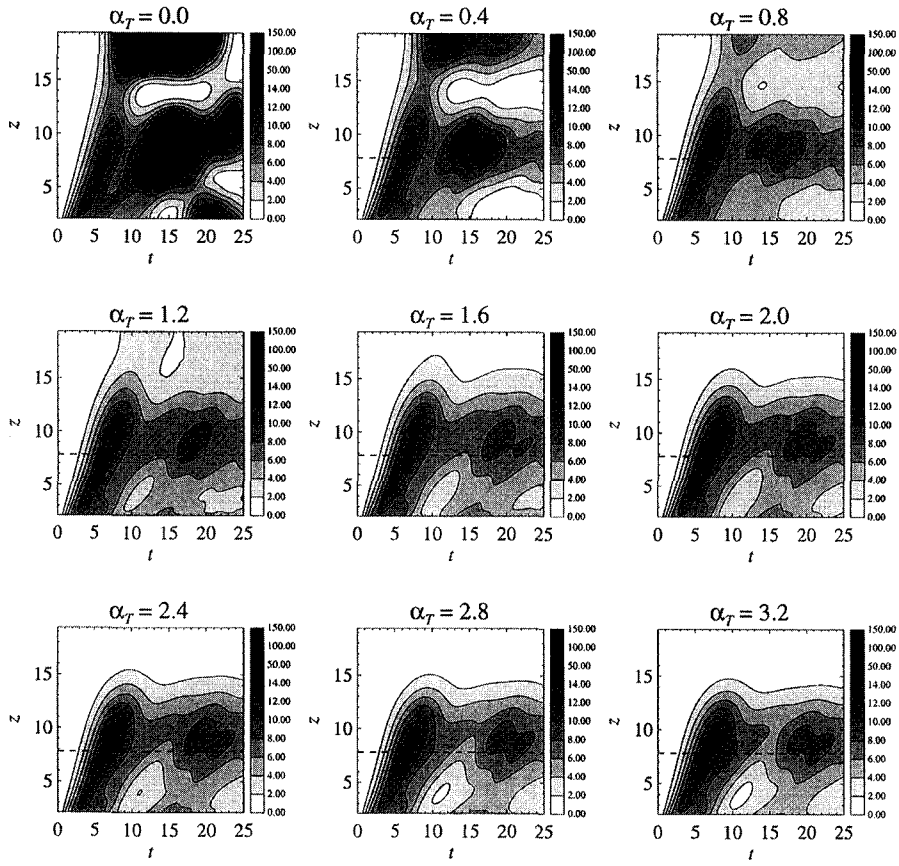

Fig. 2 Total wave activity density normalized by η_0^2 for a range of relaxation rates α_T with $\hat{z}_T = 120$ km (i.e., $z_T \approx 19.5$) and $\eta_0 = 0.15$. Where applicable the vertical sponge bottom is indicated by the horizontal dashed line. Note the nonlinear wave activity scale.

3 Main experimental results

Consider Table 1 which summarizes the various experiments conducted (over 50 in total). The main set of experiments to be discussed (in bold-type in Table 1) build upon the Boussinesq rigid upper-boundary experiments of DS, where $\eta_0 = 0.45$ or $\eta_0 = 0.6$. The plan here is to contrast wave breaking seen with and without a vertical sponge.

a *Rigid upper-boundary*

Here we consider two sets of experiments: rigid upper-boundary at 1) $\hat{z} = 48$ km (low rigid upper-boundary) and 2) $\hat{z} = 72$ km (high rigid upper-boundary). In subsequent subsections we introduce a vertical sponge in the region 48 km $\leqslant \hat{z} \leqslant 72$

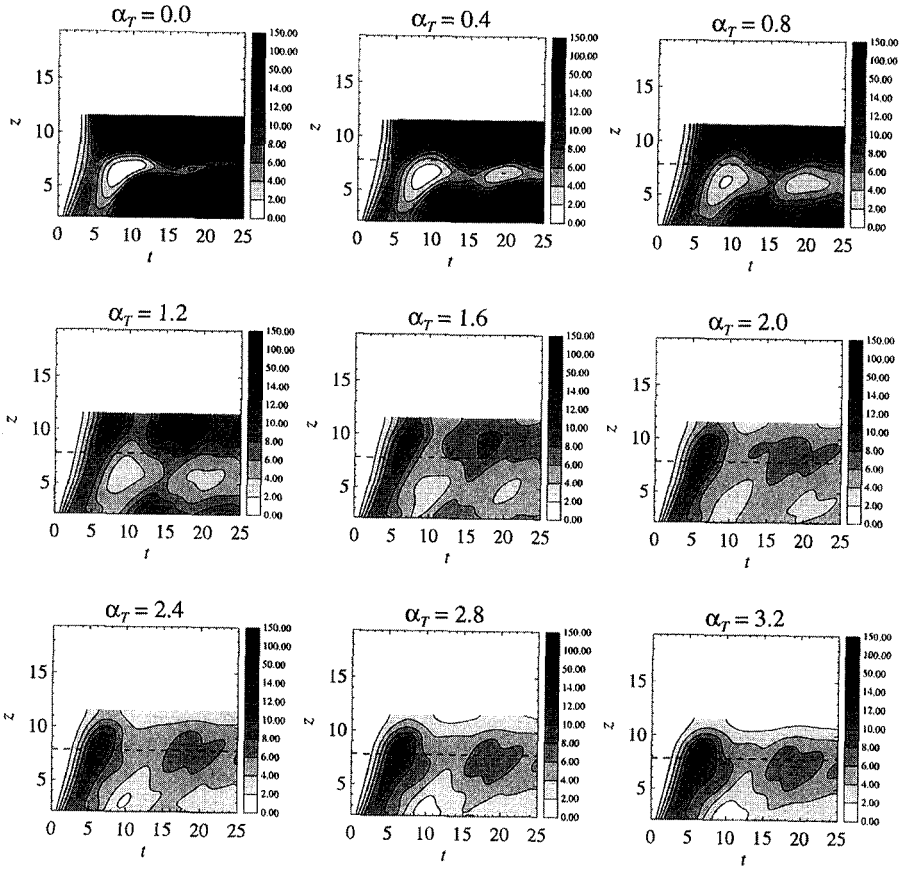

Fig. 3 As in Fig. 2 but for $\hat{z}_T = 72$ km (i.e., $z_T \approx 11.7$).

km, and so in a sense the present experiments can be considered as limiting vertical sponge cases with 1) corresponding to $\alpha_T \to \infty$ and 2) corresponding to $\alpha_T \to 0$.

1 LOW RIGID UPPER-BOUNDARY ($\mathcal{BL}$)

Consider Fig. 4 (a) and (b) which show perspective views of a weakly forced (hereafter $\mathcal{BL}_{0.45}$, $\mathcal{BL}$ standing for "Boussinesq low rigid upper-boundary" and the subscript indicating the topographic amplitude) and strongly forced (hereafter $\mathcal{BL}_{0.60}$) vortex, respectively. These are DS's $\mathcal{B}4$ and $\mathcal{B}6$ experiments respectively, using their nomenclature. To $t = 5$ the $\mathcal{BL}_{0.45}$ and $\mathcal{BL}_{0.60}$ vortices are very similar with the lower (upper) contours moving southward in the positive y-direction (x-direction). At $t = 10$ (not shown) lower-level breaking has just begun in the $\mathcal{BL}_{0.45}$ simulation but is quite advanced in the $\mathcal{BL}_{0.60}$ simulation. By $t = 15$ upper-level contour deformations dominate the $\mathcal{BL}_{0.45}$ simulation while lower-level breaking dominates the $\mathcal{BL}_{0.60}$ sim-

TABLE 1. Summary of Boussinesq experiments performed, where $\hat{z}_T$ is the dimensional domain height (km), n is the total number of levels, n_S is the number of levels in the vertical sponge (where applicable), α_T is the relaxation rate (where applicable) and η_0 is the topographic amplitude. The main set of experiments is in bold type and the identifying labels are in parentheses.

			α_T		
$\hat{z}_T$	n	n_S	$\eta_0 = 0.15$	$\eta_0 = 0.45$	$\eta_0 = 0.60$
			Rigid upper boundary		
48	20	0	0.0	**0.0** ($\mathcal{BL}_{0.45}$)	**0.0** ($\mathcal{BL}_{0.60}$)
60	26	0	0.0	0.0	0.0
72	30	0	0.0	**0.0** ($\mathcal{BH}_{0.45}$)	**0.0** ($\mathcal{BH}_{0.60}$)
96	42	0	0.0	0.0	0.0
120	54	0	0.0	•	•
144	66	0	0.0	•	•
			Vertical sponge		
60	26	6	0.8, 1.2, 1.6	0.8, 1.2, 1.6	0.8, 1.2, 1.6
72	30	12	0.4, 0.8, 1.2, 1.6	0.8, 1.2	0.8, 1.2
			2.0, 2.4, 2.8, 3.2	**1.6** ($\mathcal{BS}_{0.45}$), 2.8	**1.6** ($\mathcal{BS}_{0.60}$), 2.8
96	42	23	1.6	•	•
120	54	35	0.4, 0.8, 1.2, 1.6	•	•
			2.0, 2.4, 2.8, 3.2		

ulation. At $t = 15$ the upper-level contours in the $\mathcal{BL}_{0.45}$ simulation are stretched way out [see the plan view of the top contour (dotted) in Fig. 5(a)] while the lower-level contours are filamented [see the plan view of the bottom contour (solid) in Fig. 5(a)]. At $t = 15$ the upper-level contours in the $\mathcal{BL}_{0.60}$ simulation are relatively quiescent [see the plan view of the top contour (dotted) in Fig. 5(b)] while the lower-level contours are broken and dramatically deformed [see the plan view of the bottom contour (solid) in Fig. 5(b)]. Here, the strong lower-level breaking evidently shields the upper-level contours from the dramatic deformations seen in the corresponding $\mathcal{BL}_{0.45}$ contours (as suggested by DS). Our vertical sponge experiments to come will test which aspects of this picture are artifacts of the rigid upper-boundary condition and which are not.

Another way to look at these simulations is through height-time cross-sections of total and relative wave activity (see Fig. 6). Relative wave activity is the component of the total wave activity which is due to motions relative to the centroid of the vortex. In either the $\mathcal{BL}_{0.45}$ or $\mathcal{BL}_{0.60}$ cases we see an accumulation of total wave activity at the top of the domain up to $t \approx 5$. It is during this time that the vortex obtains its strong tilt with height as the upper-level contours shift off the pole, in the direction of low topographic heights (see Fig. 1). At $t \approx 10$ the total wave activity again builds, mostly at upper-levels in the $\mathcal{BL}_{0.45}$ simulation and at lower-levels in the $\mathcal{BL}_{0.60}$ simulation (further evidence of the shielding effect alluded to in the last paragraph). The relative wave activity plots indicate that these behaviours are due to contour shape changes as much as they are to changes in the position of the centroid of the vortex. We also note the impression of waves reflecting downwards from the top at $t \approx 5$, reaching the bottom at $t \approx 10$ and then in the $\mathcal{BL}_{0.45}$ case reflecting upwards to cause

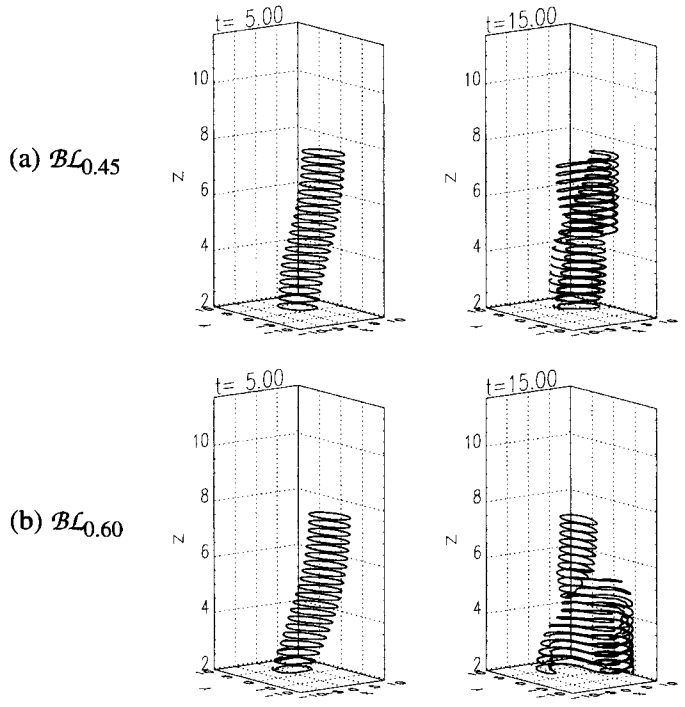

Fig. 4 Perspective views of the vortex for the case of a low rigid upper-boundary: (a) $\mathcal{BL}_{0.45}$ (weak forcing. $\eta_0 = 0.45$). (b) $\mathcal{BL}_{0.60}$ (strong forcing, $\eta_0 = 0.6$).

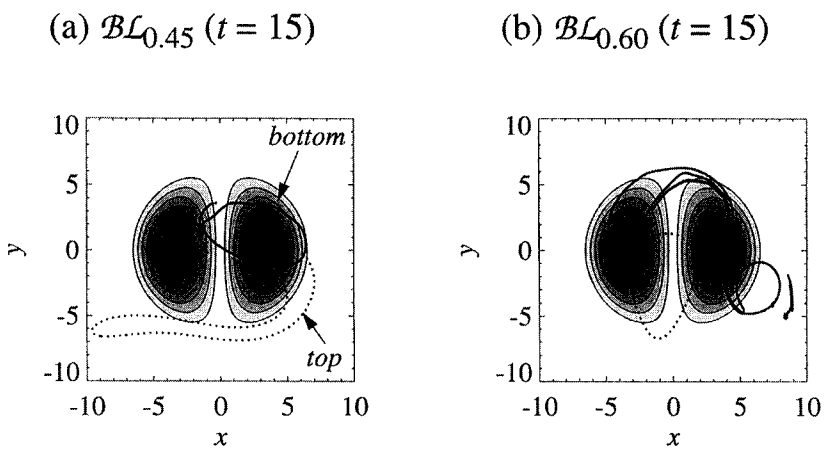

Fig. 5 Top level (dotted line) and bottom level (solid line) potential vorticity contours for the case of a low rigid upper-boundary: (a) $\mathcal{BL}_{0.45}$ ($\eta_0 = 0.45$). (b) $\mathcal{BL}_{0.60}$ ($\eta_0 = 0.6$). The topographic forcing function $-f_0\eta(x, y)$ is shaded.

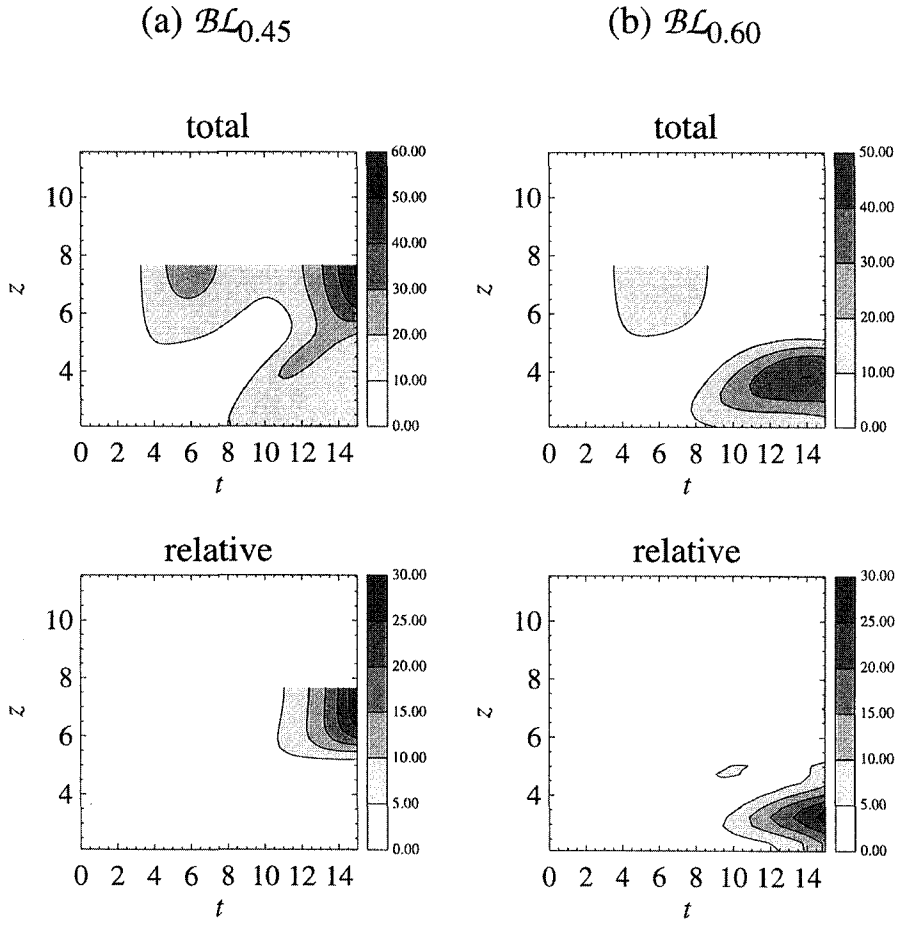

Fig. 6 Total (top) and relative (bottom) wave activity density for the case of a low rigid upper-boundary: (a) $\mathcal{BL}_{0.45}$ ($\eta_0 = 0.45$). (b) $\mathcal{BL}_{0.60}$ ($\eta_0 = 0.6$).

the subsequent upper-level havoc and in the $\mathcal{BL}_{0.60}$ case setting off the dramatic low-level breaking (and perhaps suppressing further wave propagation as suggested by DS). Further diagnostics would be required to confirm these hypothesized chains of events.

2 HIGH RIGID UPPER-BOUNDARY *($\mathcal{BH}$)*

How does the picture just painted change when the rigid upper-boundary is lifted to $\hat{z} = 72$ km? Consider Fig. 7(a) and (b) which are perspective views of a weakly forced (hereafter $\mathcal{BH}_{0.45}$, where the $\mathcal{H}$ stands for high rigid upper-boundary) and strongly forced (hereafter $\mathcal{BH}_{0.60}$) vortex, respectively, when $\hat{z}_T = 72$ km. Nothing

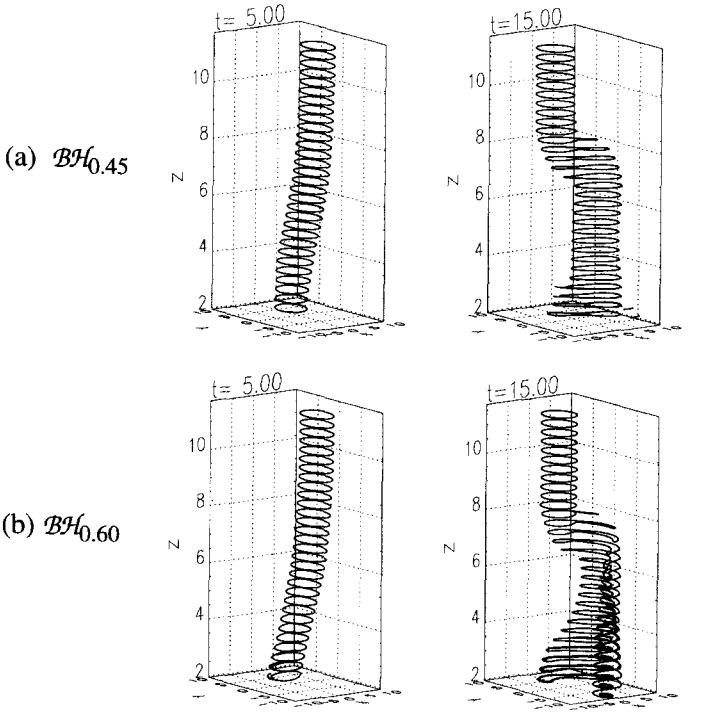

Fig. 7 As in Fig. 4 for the case of a high rigid upper-boundary: (a) $\mathcal{BH}_{0.45}$ ($\eta_0 = 0.45$). (b) $\mathcal{BH}_{0.60}$ ($\eta_0 = 0.6$).

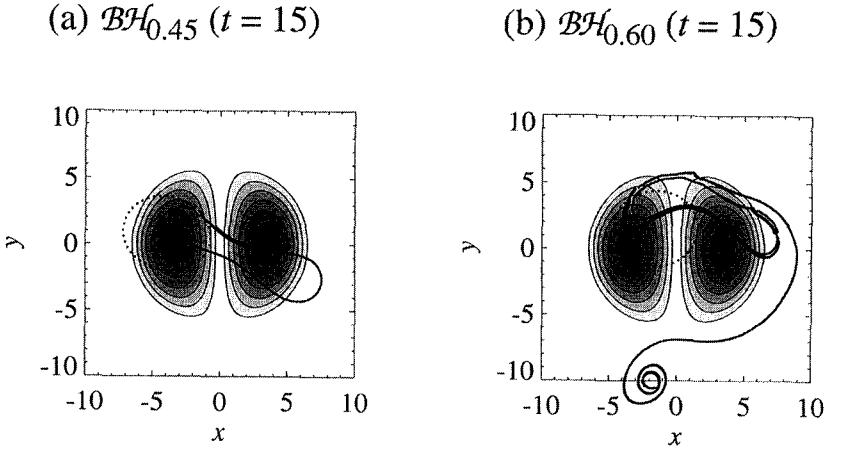

Fig. 8 As in Fig. 5 for the case of a high rigid upper-boundary: (a) $\mathcal{BH}_{0.45}$ ($\eta_0 = 0.45$). (b) $\mathcal{BH}_{0.60}$ ($\eta_0 = 0.6$).

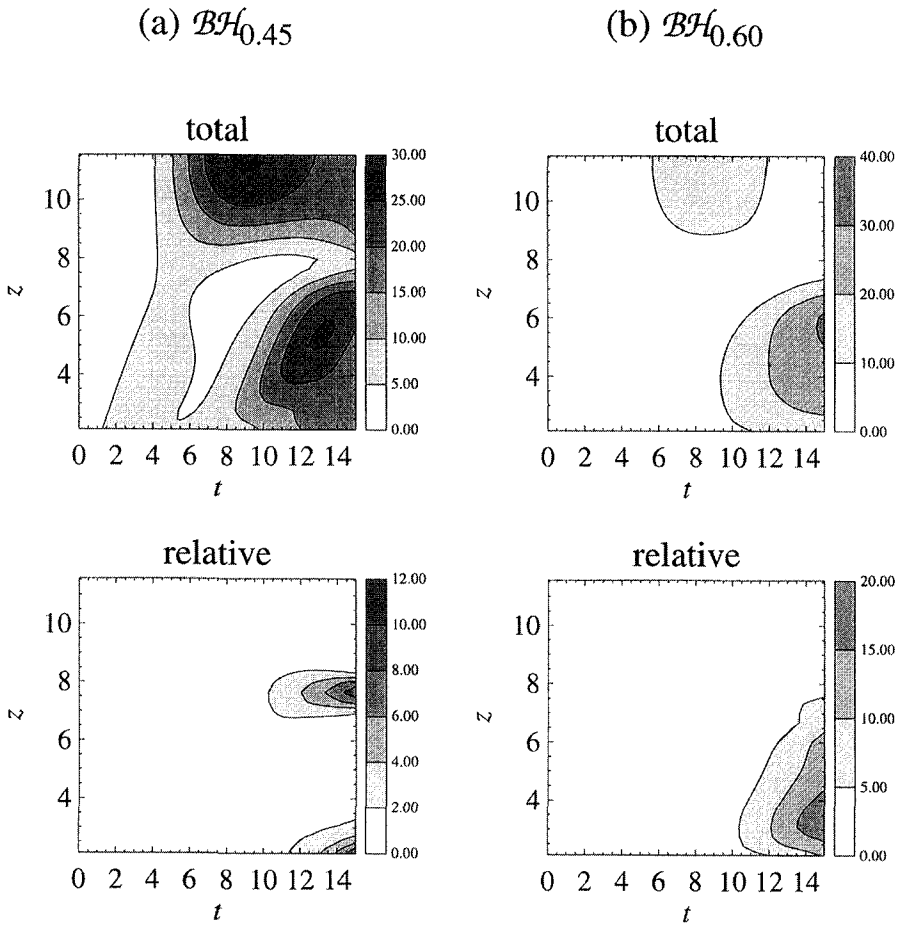

Fig. 9 As in Fig. 6 for the case of a high rigid upper-boundary: (a) $\mathcal{BH}_{0.45}$ ($\eta_0 = 0.45$). (b) $\mathcal{BH}_{0.60}$ ($\eta_0 = 0.6$).

appreciably different from the lower upper-boundary case happens to the vortex before $t \approx 5$, whether weakly or strongly forced. After $t \approx 5$ the $\mathcal{BH}_{0.60}$ vortex evolves much as the $\mathcal{BL}_{0.60}$ one, in the sense that the breaking is confined to the lower half of the domain and is very complex [i.e., involving vortex displacement, reshaping, filamentation and secondary development (compare Fig. 8(b) and Fig. 5(b) solid lines)]. On the other hand, after $t \approx 5$ the $\mathcal{BH}_{0.45}$ vortex evolves much differently than the $\mathcal{BL}_{0.45}$ case insofar as the former's upper-level contours undergo relatively little shape change [compare Fig. 8(a) and Fig. 5(a), dashed lines]. We note in the $\mathcal{BH}_{0.45}$ case, and subsequent to $t \approx 15$ (not shown), that two distinct regions of breaking develop, one near a kink in the vortex at $z \approx 7.5$ and another near the bot-

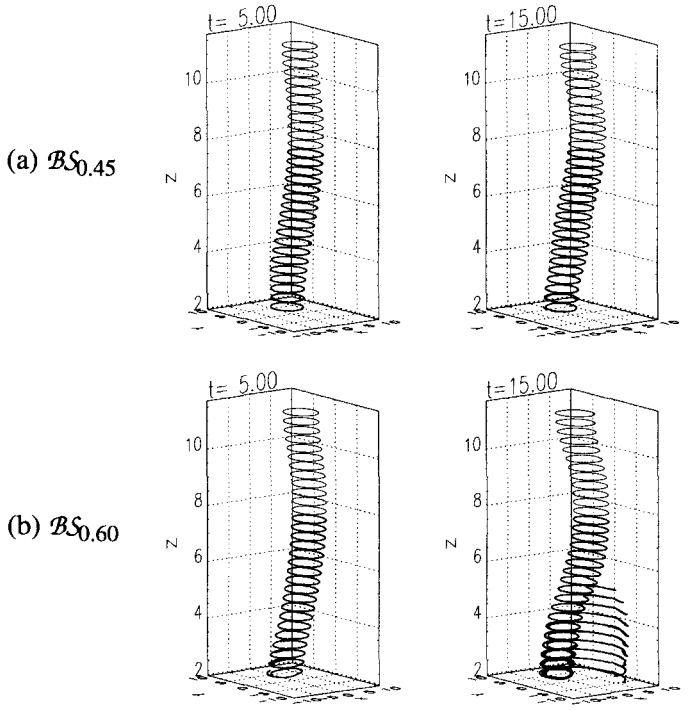

Fig. 10 As in Fig. 4 for the case of a vertical sponge (α_T = 1.6): (a) $\mathcal{BS}_{0.45}$ (η_0 = 0.45). (b) $\mathcal{BS}_{0.60}$ (η_0 = 0.6). The thin solid contours are contours within the vertical sponge.

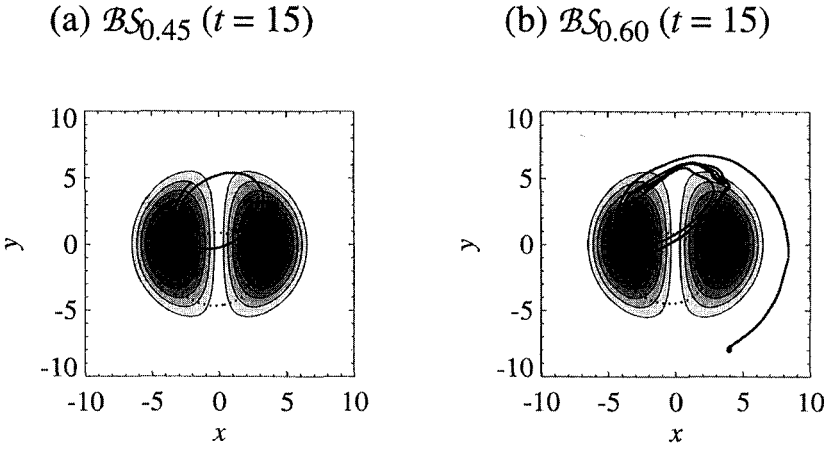

Fig. 11 As in Fig. 5 for the case of a vertical sponge (α_T = 1.6): (a) $\mathcal{BS}_{0.45}$ (η_0 = 0.45). (b) $\mathcal{BS}_{0.60}$ (η_0 = 0.6).

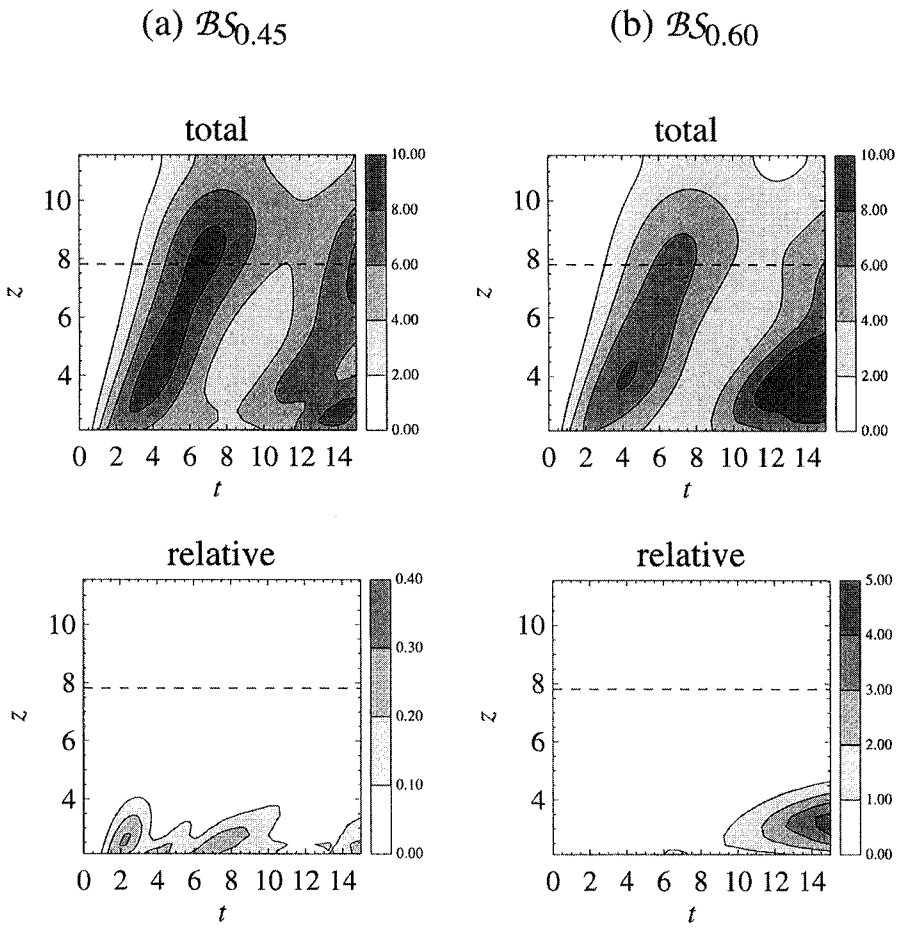

Fig. 12 As in Fig. 6 for the case of a vertical sponge ($\alpha_T = 1.6$): (a) $\mathcal{BS}_{0.45}$ ($\eta_0 = 0.45$). (b) $\mathcal{BS}_{0.60}$ ($\eta_0 = 0.6$). The vertical sponge bottom is indicated by the horizontal dashed line.

tom. An early hint of this behaviour is seen in the bottom left panel of Fig. 9 which shows relative wave activity maxima at $z \approx 7.5$ and $z \approx z_B$ beginning around $t = 10$.

b *Vertical sponge ($\mathcal{BS}$)*

Let us now consider placing a vertical sponge in the region 48 km $\leqslant \hat{z} \leqslant$ 72 km. Comparing Fig. 10 and Fig. 7 there appears little difference between the $\mathcal{BH}$ (high rigid upper-boundary) and the $\mathcal{BS}$ (vertical sponge) cases up to $t \approx 5$ (i.e., with or without a vertical sponge the vortex is tilted with height and there is some minor low-level breaking when strongly forced). Beyond $t \approx 5$ the evolution is quite different. For example, the $\mathcal{BS}_{0.45}$ vortex [Fig. 10(a) and Fig. 11(a)] remains in a more

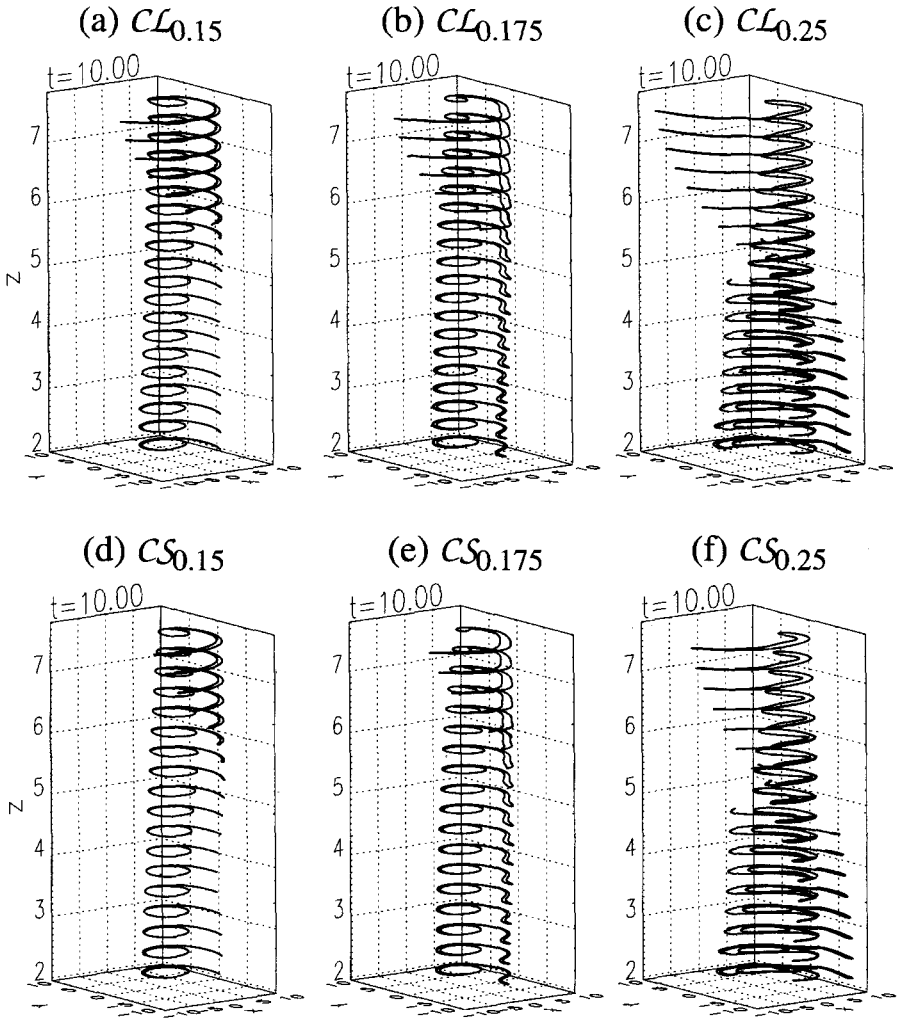

Fig. 13 Perspective view of the vortex for a compressible vortex: Low rigid upper-boundary cases: (a) $CL_{0.15}$ ($\eta_0 = 0.15$), (b) $CL_{0.175}$ ($\eta_0 = 0.175$) and (c) $CL_{0.25}$ ($\eta_0 = 0.25$). Vertical sponge cases: (d) $CS_{0.15}$ ($\eta_0 = 0.15$), (e) $CS_{0.175}$ ($\eta_0 = 0.175$) and (f) $CS_{0.25}$ ($\eta_0 = 0.25$). Note that the plots do not include the region of the vertical sponge.

or less steady state (excepting some relatively minor low-level breaking) to $t \approx 15$ (and in fact to the end of the simulation at $t = 25$, not shown). On the other hand, the corresponding $\mathcal{BH}_{0.45}$ vortex [Fig. 7(a) and Fig. 8(a)] shows advanced breaking and/or contour distortion throughout the lower two-thirds of the domain during the same time. The $\mathcal{BS}_{0.60}$ [Fig. 10(b) and Fig. 11(b)] and $\mathcal{BH}_{0.60}$ [Fig. 7(b) and Fig.

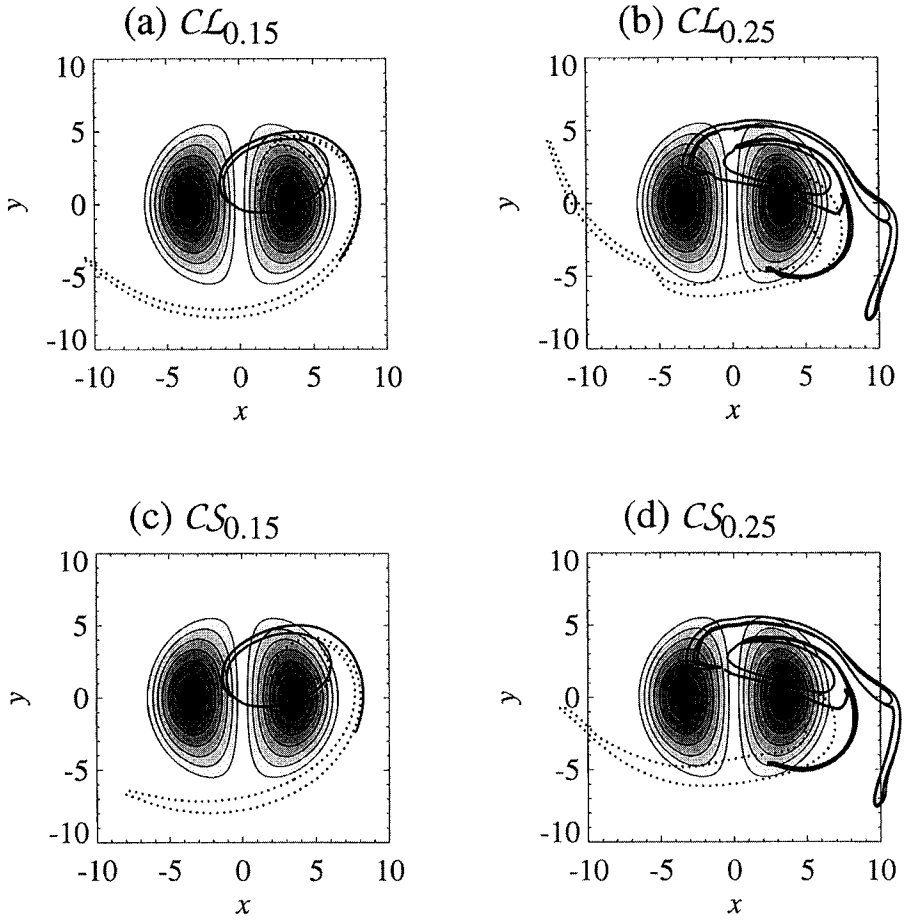

Fig. 14 Top level (dotted line) and bottom level (solid line) potential vorticity contours: Low rigid upper-boundary cases: (a) $\mathcal{CL}_{0.15}$ ($\eta_0 = 0.15$) and (b) $\mathcal{CL}_{0.25}$ ($\eta_0 = 0.25$). Vertical sponge cases: (c) $\mathcal{CS}_{0.15}$ ($\eta_0 = 0.15$) and (d) $\mathcal{CS}_{0.25}$ ($\eta_0 = 0.25$).

8(b)] simulations are also quite different. Although both simulations exhibit significant lower-level breaking, the character of the breaking is quite different. Specifically, the $\mathcal{BS}_{0.60}$ vortex remains more or less intact despite winding and then expulsion of a thin and seemingly passive filament. The $\mathcal{BH}_{0.60}$ vortex, on the other hand, shows a much less recognizable main vortex and the development of a secondary vortex. For completeness we show the $\mathcal{BS}$ wave activity plots in Fig. 12, which when compared to the corresponding $\mathcal{BH}$ plots in Fig. 9 further punctuates our point that the evolution of a barotropic vortex can be highly sensitive to the upper boundary condition.

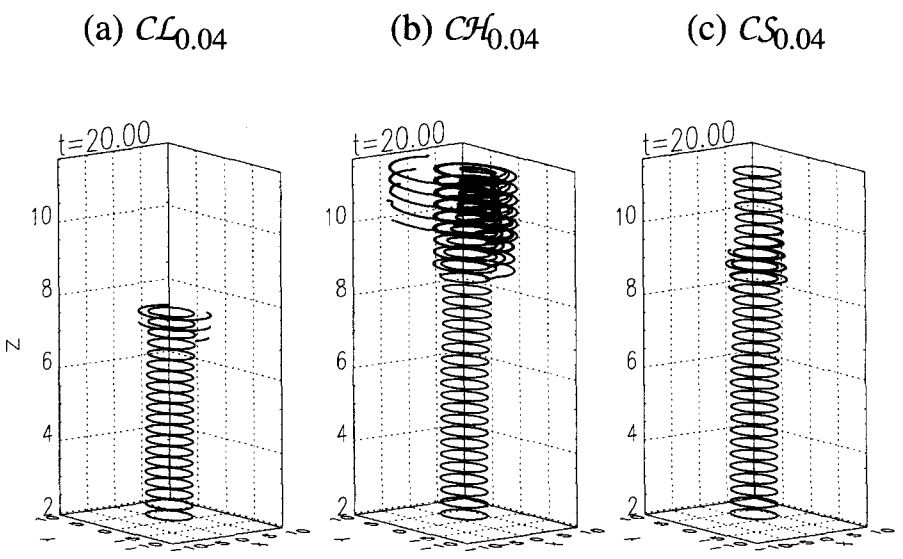

Fig. 15 Perspective views of a compressible vortex for a very weak forcing amplitude of $\eta_0 = 0.04$. (a) Low rigid-lid $CL_{0.04}$. (b) High rigid-lid $CH_{0.04}$. (c) Vertical sponge $CS_{0.04}$.

4 Summary and discussion

This study was primarily motivated by DS who used a three-dimensional quasi-geostrophic contour dynamics/surgery numerical model to study the response of a barotropic vortex to topographic forcing of varying amplitude. Our specific question, in the context of DS, is what is the role of the rigid upper-boundary condition in wave breaking? We have addressed this question by replacing the rigid upper-boundary with a vertical sponge. Our main results are:

- Given a vertical sponge and a forcing amplitude greater than a certain critical value, breaking is as in the corresponding rigid upper-boundary case insofar as it is confined to the lower half of the vortex. However, important differences exist. For example, with a vertical sponge the vortex remains fairly true to its initial circular shape but is wrapped by a long narrow filament at lower levels. Without a vertical sponge the vortex is so deformed at lower levels as to be nearly unrecognizable. We caution the reader that while interesting in itself we have not shown this to be a general result, that is to say there does exist the possibility that for yet larger forcing amplitudes the lower level vortex could be destroyed even in the presence of an absorbing sponge.
- Given a vertical sponge and a forcing amplitude less than the critical value no breaking exists. This contrasts with the rigid upper-boundary case which shows significant deformations near the upper boundary. Evidently the upper level deformations are an artifact of the rigid upper-boundary condition.

Our conclusions so far are based on the assumption of a constant density profile. Given a more realistic density profile [say, $\rho_0(z) = \rho_{00} \exp(-z/H)$] the degree to which our results hold will depend upon the point at which wave amplitudes become large enough, due to the density effect, to break. If that point is situated well above the model domain then our Boussinesq results should hold to first approximation. If, on the other hand, that point lies within the model domain our conclusions will have to be modified. Take, for example, Fig. 13(a)–(c) which shows a series of experiments with an exponential density profile and a rigid-lid located just above the top-most contour (as considered in DS). To judge whether or not the upper-level breaking is due to the density effect (i.e., wave amplitudes increasing exponentially with height) or the rigid-lid effect (discussed earlier) we repeat this set of simulations but with our absorbing sponge replacing DS's rigid-lid [see Fig. 13(c)–(e)]. Given the close correspondence between the rigid-lid and absorbing sponge simulations we conclude that for this range of forcing amplitudes the density effect dominates the upper-level response, with upper-boundary specification playing only a minor role (consider also Fig. 14 for the corresponding plan views). Further in this vein, consider Fig. 15 where, given a much reduced topographic amplitude, we contrast a low rigid-lid [Fig. 15(a)], high rigid-lid [Fig. 15(b)] and absorbing sponge [Fig. 15(c)] simulation. For this topographic forcing it appears that the density-effect only becomes significant within the region of the sponge. The upper-level breaking seen in the low rigid-lid experiment is therefore interpreted as a local amplification due to boundary reflections (as in our small amplitude Boussinesq simulations).

Acknowledgments

The authors are grateful to R. Saravanan for providing the contour dynamics/surgery computer code and for many useful discussions, and to G. Boer, C. Reader, I. Fung and M. Holzer for helpful review comments. Alan Plumb and two other reviewers are thanked for their very constructive reviews. Funding for this research is through the Climate Research Network of the Atmospheric Research Service.

References

ANDREWS, D.G., J.R. HOLTON, and C.B. LEOVY. 1987. *Middle Atmosphere Dynamics*. Academic Press, 489 pp.

DRITSCHEL, D.G. 1988. Contour Surgery: a topological reconnection scheme for extended integrations using Contour Dynamics. *J. Comput. Phys.* **77**: 240–266.

———. 1989. Contour Dynamics and Contour Surgery: numerical algorithms for extended, high-resolution modelling of vortex dynamics in two-dimensional, inviscid, incompressible flows. *Comput. Phys. Rep.* **10**: 77–146.

——— and R. SARAVANAN. 1994. Three-dimensional quasi-geostrophic Contour Dynamics with an application to stratospheric vortex dynamics. *Q.J.R. Meteorol. Soc.* **120**: 1267–1297.

DUNKERTON, T.J. 1981. Wave transience in a compressible atmosphere. Part I: Transient internal wave, mean-flow interaction. *J. Atmos. Sci.* **38**: 281–297.

FYFE, J. and I.M. HELD. 1990. The *two-fifths* and *one-fifth* rules for Rossby wave breaking in the WKB limit. *J. Atmos. Sci.* **47(6)**: 697–706.

PEDLOSKY, J. 1987. *Geophysical Fluid Dynamics.* Springer-Verlag, 710 pp.

POLVANI, L.M. and R.A. PLUMB. 1992. Rossby wave breaking, microbreaking, filamentation, and secondary vortex formation: the dynamics of a perturbed vortex. *J. Atmos. Sci.* **49(6)**: 462–476.

WAUGH, D.W. 1993. Contour surgery simulations of a forced polar vortex. *J. Atmos. Sci.* **50(5)**: 714–730.